WILEY

| RESEARCH ARTICLE

Mapping River Bed Topography in Whitewater Rapids Using Bathymetric LiDAR

Jan Rhomberg-Kauert[1] | Theresa Himmelsbach[2] | Florian Pöppl[1,3] | Lucas Dammert[1] | Martin Pfennigbauer[4] | Gottfried Mandlburger[1]

[1]Department of Geodesy and Geoinformation, TU Wien, Vienna, Austria | [2]Unit of Hydraulic Engineering, Universität Innsbruck, Innsbruck, Austria | [3]RIEGL Laser Measurement Systems GmbH, Austria | [4]RIEGL Research and Defense GmbH, Austria

Correspondence: Jan Rhomberg-Kauert (jan.rhomberg-kauert@geo.tuwien.ac.at)

ABSTRACT

Bathymetric LiDAR captures river topography efficiently for clear and shallow water, but for mountain rivers, whitewater rapids still pose challenges. This study proposes a novel method to enable the extraction of bottom returns specifically in turbulent whitewater sections. The method outlined uses a curve fitting approach to subtract the water column from the recorded LiDAR waveform, calculates a residual of reflected energy that is not attributed to the water column, and applies peak detection on the residual to extract previously undetected returns. For the evaluation of the points derived from the additional returns, three different rivers were surveyed with both LiDAR measurements and a total station with a reflector pole. This provides the foundation for assessing the accuracy of the new underwater terrain points. Compared to the reference data, this results in a median reduction in the distance to the reference points from 20.6 to 9.2 cm and 40.4 to 22.5 cm. Because it closes significant gaps in the data where no bottom points were detected. In conclusion, this study extends the application of full-waveform processing for bathymetric LiDAR to whitewater rivers, which opens up the field of bathymetric LiDAR for river research in the turbulent environment of mountain rivers.

1 | Introduction

River bathymetry forms the basis for hydrodynamic numerical modeling, morphodynamic change detection, flood hazard mapping, examination of sediment transport processes, and for ecohydraulic topics such as habitat modeling or river restoration (Farò et al. 2023; Mandlburger et al. 2009; Wohl et al. 2015). Thus, the field of riverbed surveying has experienced significant advances in recent decades, particularly through the introduction of remote sensing techniques, which have greatly improved the data quality in terms of spatial coverage and point density (Kinzel et al. 2012; Mandlburger et al. 2023; Pfennigbauer et al. 2011; Piégay et al. 2019).

Today, there are many different approaches to capture river bathymetry, including in situ surveys and different remote sensing measurements (Bio et al. 2020; Kim and Ryou 2020; Lee et al. 2022; Mandlburger et al. 2023; Pan, Glennie, Legleiter, and Overstreet 2015; Piégay et al. 2019; Tomsett and Leyland 2019). Depending on the scale of the surveyed area, remote sensing techniques range from satellite-based imagery to sonar, airborne photogrammetry, and light detection and ranging (LiDAR) measurements, deployed from planes, helicopters, unmanned aerial vehicles (UAVs) or unmanned surface vehicles (USVs) (Lee et al. 2022; Kim and Ryou 2020; Mandlburger et al. 2023; Moramarco et al. 2019; Tomsett and Leyland 2019). Satellite-based imagery can only provide low spatial resolution

(minimum 30 cm pixels), suitable for larger bodies of water (Hartmann et al. 2021). Therefore, in smaller rivers common methods employed are SONAR and (topo-)bathymetric LiDAR (Lague and Feldmann 2020; Mandlburger et al. 2023; Sundt et al. 2021).

However, not all remote sensing methods can be applied to all types of rivers (Tomsett and Leyland 2019). One of the types is mountain rivers. Mountain rivers typically have rough river beds with a large variability in grain sizes up to immobile boulders, which, depending on the slope, can form step-pool sequences (Buffington and Montgomery 2021). Together with the shallow flow depth, the morphological structures lead to an abrupt transition in flow regimes from super- to subcritical flows, resulting in energy-dissipating hydraulic jumps visible as whitewater rapids (Pagliara et al. 2008; Magirl et al. 2009).

Whitewater rapids make mountain rivers ecologically valuable habitats (Papadaki et al. 2016; Wheaton et al. 2009). However, they are a limiting factor for most surveying techniques (Magirl et al. 2009; McMahon 1981). For terrestrial survey methods, which require wading into the water with a measurement device, such as a prism pole tracked by a total station or measurements with global navigation satellite systems (GNSSs), whitewater rapids are dangerous river sections, making them either impossible to enter or very difficult to measure accurately (Strom et al. 2017). While the risk of drowning and injury poses major obstacles to surveys, a secondary minor challenge towards high accuracy measurement is the force of the water acting upon the reflector pole, as this introduces uncertainty in the position of the measured points.

Mountain rivers, with their shallow flow depth, are generally not suitable for boat or USV-based SONAR (Jawak et al. 2015; Kim and Ryou 2020), and more generally, such rough shallow waters tend to produce noisy SONAR data due to the higher beam angle (Kastdalen et al. 2024).

Considering the often difficult accessibility of mountain rivers and the presence of large boulders that hinder water surface surveys, methods are gradually changing to aerial or UAV-based remote sensing (Li et al. 2022). Although UAV-based images deliver high-resolution data of dry river banks, the resulting point clouds of turbulent water surfaces are highly variable and cannot deliver bathymetry data for sections of air-water mixture in whitewater rapids (Dufficy et al. 2024). Such challenges further extend to common photogrammetric approaches (Dietrich 2016; Woodget et al. 2017), as feature matching is limited primarily to water surface points. Thus, airborne or UAV-borne topo-bathymetric LiDAR has become a common method used in gravel-bed rivers (Dey et al. 2019; Lague and Feldmann 2020; Mandlburger et al. 2015), but has hardly been applied to rivers with mountain river characteristics (Ferguson et al. 2024; Tonina et al. 2020; Wiener and Pasternack 2022). Whitewater limitations with regard to topo-bathymetric LiDAR have been acknowledged in the literature (Lague and Feldmann 2020; Kastdalen et al. 2024), but topo-bathymetric LiDAR has mainly been applied in water bodies with moderate complexity of the river morphologies and for water depths well above 20 cm (Frizzle et al. 2024; Kinzel et al. 2021).

In the last decade, advances in LiDAR software and hardware have improved the quality and resolution of underwater data (Chauve et al. 2007; Mandlburger et al. 2023; Pfennigbauer et al. 2011). The introduction of full-waveform LiDAR systems, which are capable of recording the full temporal record of the reflected laser pulse, has enabled the development of specialized signal processing methods (Ullrich and Reichert 2005; Mader et al. 2021; Pfennigbauer et al. 2011; Schwarz et al. 2019). Here, the relative difference to online signal processing applications is that instead of immediately analyzing received signals for echo pulse detection (Pfennigbauer et al. 2009), the entire shape of the reflected echo of each laser pulse is stored (Ullrich and Reichert 2005). This allows for the extraction of more information from the LiDAR signal than just the peak. Two commonly cited methods are peak detection-based algorithms (Chauve et al. 2007; Mallet and Bretar 2009; Pfennigbauer et al. 2009, 2022) and the surface-volume-bottom (SVB) algorithm (Schwarz et al. 2019; Schwarz and Pfennigbauer 2024). The latter uses a physical model of the interaction between the laser pulse and the water column to improve point detection. Furthermore, specialized tools that exceed the processing of a single waveform have been shown to improve bottom echo detection, namely waveform averaging (Pan, Glennie, Hartzell, et al. 2015; Pfennigbauer et al. 2011; Mader et al. 2021). Through the combination of multiple waveforms of close spatial proximity into a single waveform, the overall signal-to-noise ratio is increased, allowing the detection of weaker echoes (Pfennigbauer et al. 2011; Mader et al. 2021).

Current research on topo-bathymetric LiDAR for whitewater has focused mainly on air-water flows (Hall et al. 2012; Li et al. 2019, 2022) or underlined the challenges in the whitewater section (Awadallah et al. 2023; Skinner 2011). Among these challenges are the hazardous environment for personnel, fast and shallow waters hindering SONAR measurements, and sparse penetration of LiDAR through the whitewater (Awadallah et al. 2023; Skinner 2011). However, previous studies have not provided methodologies to improve full-waveform processing. Therefore, this study aims to extend current LiDAR processing methodologies to capture terrain points within whitewater rapids. The goal is to improve automated terrain mapping of mountain rivers and to increase the spatial coverage of bathymetry data for mountain rivers.

In our study, we first introduce three river datasets (Section 2), where we use a well-researched pre-alpine river in Lower Austria as a reference dataset and two mountain rivers located in the central Alps as test sites. Based only on the reference dataset, we present the fundamental techniques used for the full-waveform LiDAR analysis (Section 3) and introduce a minimal parameter curve fitting for the LiDAR interaction with the water column (Section 3.1.2). This approximation of the LiDAR waveform can then be used to extract additional points from the whitewater waveforms by analyzing the differences in energy between the recorded laser pulse (as a full-waveform) and the theoretical return based on the curve fitting (Section 3.2). Our method is applied to each waveform that produces a water surface point. For each waveform, curve fitting is applied and, if successful, the residual is calculated. For these residuals, peak detection (Virtanen et al. 2020)

extracts potential whitewater bottom returns, filtered by distance from the water surface (greater than 20 cm), minimal horizontal distance to the next peak of the waveform (approximately 8 ns) and echo number (must be the second echo). The newly extracted points are then evaluated against the measured reference data from river transects. In this way, we rigorously assess the method (Section 4) and thoroughly discuss the results obtained (Section 5).

2 | Materials

The presented study consists of multiple areas (Pielach [Austria], Fischbach [Austria], and Passer [Italy]) and different types of data (full-waveform LiDAR and reference measurements). The differences between the sites and the extent of the data are outlined in this section, providing the materials for the intended analysis, as well as the required background.

2.1 | Surveyed Areas

The Pielach is a pre-alpine river that has retained natural self-forming morphological characteristics and has a mean flow rate of 6.5 m^3/s with almost no whitewater (Mandlburger et al. 2015; Panchan et al. 2022). In contrast to the Pielach River, both the Passer and Fischbach River can be characterized as mountain rivers with steep slopes of 2% and 8% inclination, respectively, broad grain size distributions including large immobile boulders, and numerous whitewater sections. The Passer River has a plane-bed morphology and a mean discharge of about 11.5 m^3/s. The Fischbach River has a step-pool morphology with a average discharge of about 3.5 m^3/s. These differences can be seen both in the general area around the surveyed sites and in the orthophotos of the representative sections shown in Figure 1. The Pielach River is later used as a reference dataset for the waveform fitting, as it is a standard measurement environment with an extensive reference measurement coverage (Mandlburger et al. 2025). This allows us to establish our methodology first on a lower-slope gravel-bed river section and then apply the gained insights to whitewater rapids and extend the scope of what is currently considered viable for LiDAR bathymetry.

2.2 | Datasets

Each site was surveyed with a bathymetric laser scanner mounted on a UAV platform. In all cases, the system used was a *RIEGL* VQ-840-GL topo-bathymetric laser scanner with a wavelength of 532 nm and full-waveform recording. In more detail, the average laser footprint on the ground ranged from around 6 cm for the Pielach study site to approximately 20 cm for the mountain rivers according to the selected scanner settings (Table 1). The difference in flight altitudes between the Pielach study site and the mountain rivers is mainly driven by external circumstances. The region of Lower Austria experienced a major flood event in September 2024 (Blöschl 2024; Rhomberg-Kauert et al. 2025). Therefore, this site was mapped at a higher detail and with a different focus in mind during data acquisition, and here only serves as a reference dataset.

For each laser scan, the data was processed using the SVB algorithm and exported as a point cloud in a georeferenced coordinate system (ETRS89, UTM33N; EPSG: 25833) for the Pielach River or a local project coordinate system (PCS) for the mountain rivers.

The reference data for the three river datasets consists of in situ measurements recorded by a two-person team using a total station and a reflector pole. For all three study sites, the registration between the LiDAR point cloud and reference measurements was achieved using alignment reference objects (e.g., planes).

For each site, a representative cross section is shown in Figure 2A,C,E corresponding to the orthophotos of Figure 1, together with a selection of the waveforms recorded in the center region of the cross section (Figure 2A,D,F).

2.3 | Data Preprocessing

LiDAR data tend to be noisy, especially for bathymetric LiDAR, as the water column backscattering introduces a high amount of noise due to multipath effects and unwanted echoes reflected by suspended sediment. Thus, the outlier removal selected for data cleaning in this study is a clustering approach, using density-based clustering (DBSCAN) with an epsilon parameter of 0.3 (Ester et al. 1996; Schubert et al. 2017; Pedregosa et al. 2011), similar to previous studies (Rhomberg-Kauert, Dammert, et al. 2024).

3 | Methods

To extend current full-waveform LiDAR processing toward the application in whitewater rapids (Figure 3), we first build a theoretical framework of the LiDAR interaction with the water column by convoluting a Gaussian pulse with an exponential decay function. This idealized bathymetric LiDAR waveform can then be fitted to the averaged waveform to outline general trends for the laser-water interaction in whitewater rapids (Figure 3—analysis of combined waveforms). Second, we apply the theoretical model to the individual whitewater waveforms using curve fitting and perform an analysis of the difference between the idealized laser–water interaction and the recorded waveform (Figure 3—analysis of individual waveforms) from which the new points can be extracted.

3.1 | Analysis of Combined Waveforms

To analyze the different waveforms at all three study sites, we introduce two main tools: First, waveform averaging, which combines multiple waveforms into a single generalized one. Second, the curve fitting of a water column backscattering function. Waveform averaging is used to outline the general characteristics of similar laser pulses with close spatial proximity. The curve fitting represents an idealized interaction of the laser pulse with the water column, based on the water column backscattering given by the convolution of a Gaussian pulse with an
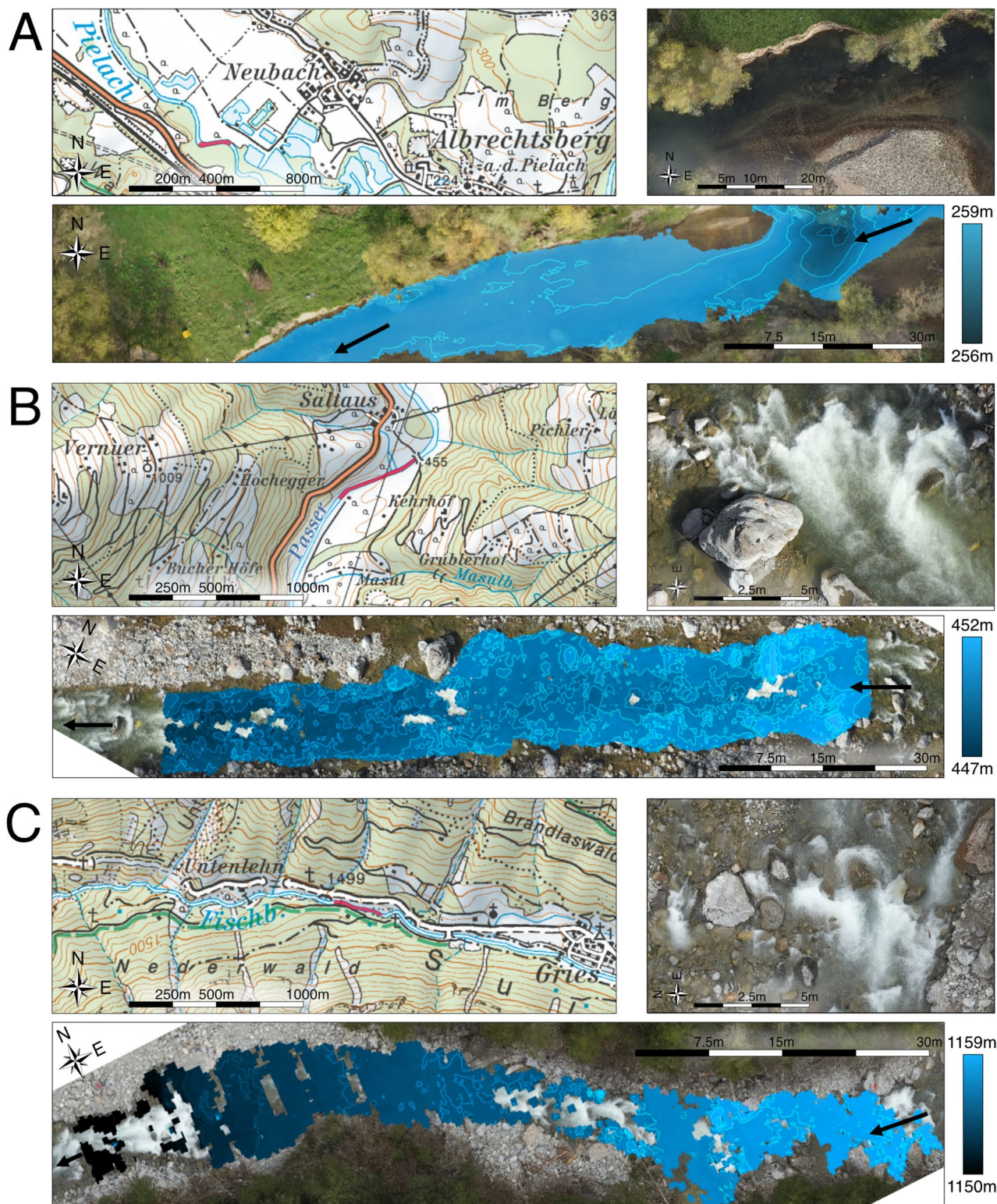
FIGURE 1 | Overview of the study sites (red area), orthophotos of three representative regions of each site (BEV 2024) and digital terrain model (20 cm resolution) overlaid on the orthophoto. (A) Pielach River (48.2153° N, 15.3732° E) in Lower Austria (Austria), (B) Passer River (46.7264° N, 11.2010° E) in South Tyrol (Italy), and (C) Fischbach River (47.0728° N, 11.0070° E) in Tyrol (Austria). [Color figure can be viewed at wileyonlinelibrary.com]

exponential decay function. In our study, waveform averaging is used to identify the general waveform behavior (Section 4.1) while curve fitting is used for the whitewater point extraction (Section 4.2).

3.1.1 | Waveform Averaging

The underlying idea of waveform averaging is to combine multiple waveforms into a single waveform. However, under

TABLE 1 | Different settings and parameters of the LiDAR systems used in the surveys.

Location	Sensor	Flight altitude	Beam divergence
Pielach	*RIEGL* VQ-840-GL	$60 \pm 5\,m$	1 mrad
Passer	*RIEGL* VQ-840-GL	$106 \pm 10\,m$	2 mrad
Fischbach	*RIEGL* VQ-840-GL	$102 \pm 14\,m$	2 mrad
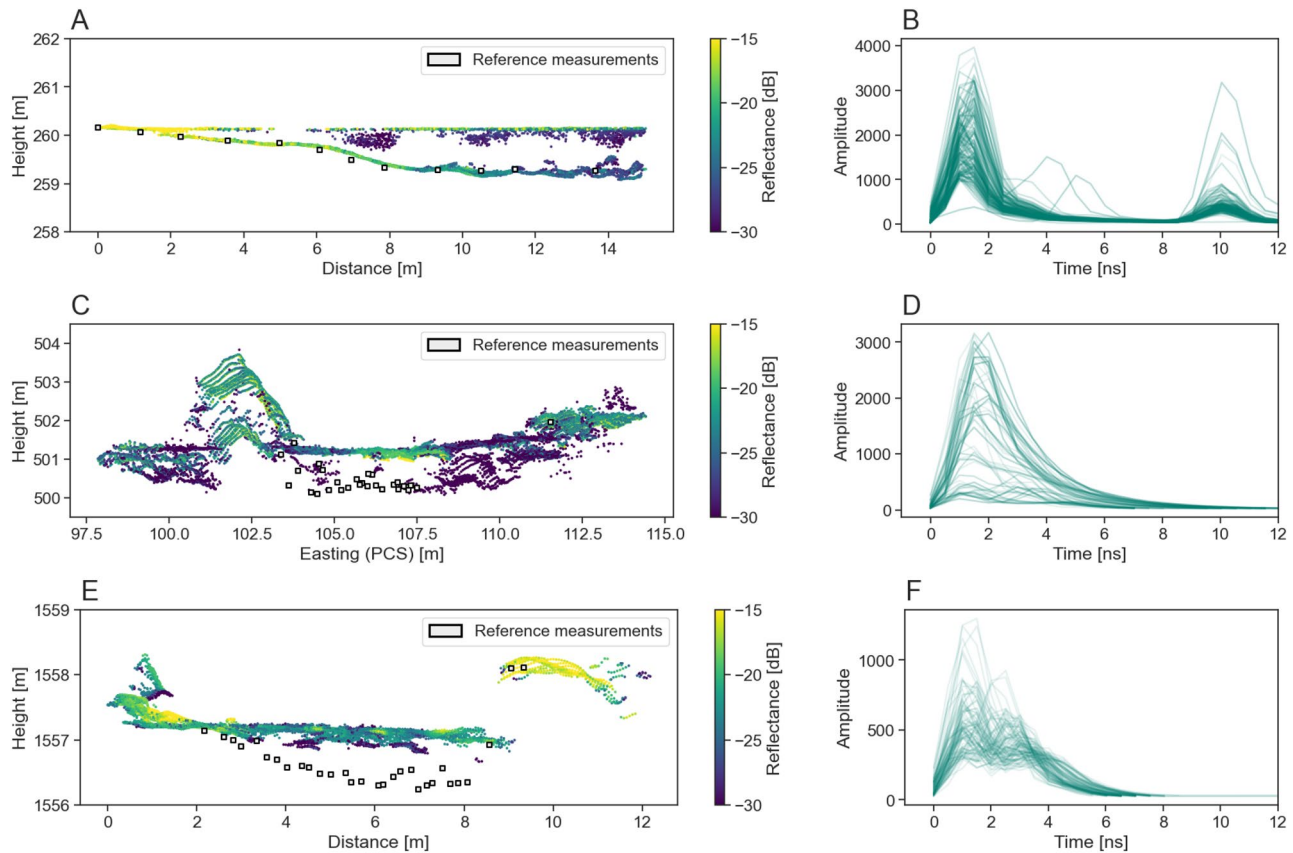
FIGURE 2 | Cross sections of the three sections for each study, together with the recorded full-waveform data of the LiDAR system. The waveforms are extracted in the center of each cross section and set to start at zero. [Color figure can be viewed at wileyonlinelibrary.com]

real-world conditions, waveforms tend to display variations even in similar settings. Therefore, the waveforms have to first be efficiently combined. The first step is to select an area of similar terrain or waveforms of approximately equal shape. For example, a similar distance between the water surface and bottom, with a flat water surface and even terrain, as is the case for parts of the Pielach dataset. In the mountain rivers, a similar selection is achieved by combining waveforms of similar maximum amplitude.

As the LiDAR system is not stationary, the distance from the scanner to the water surface varies. Because the selected waveforms have the same distance within the water, they can effectively be aligned by setting the starting time of the recorded waveform (the laser pulse hitting the water) to zero. Since all waveforms have the same start and are similar in shape, we get a distribution of waveforms that looks similar to the scatterplot in Figure 4. Each combined time stamp has a variety of amplitudes corresponding to the input waveforms, and an average value can be calculated for each

time stamp (Figure 4). To extract the final, averaged waveform, the last step in the waveform averaging workflow is the interpolation between the averaged amplitudes to obtain a smooth curve.
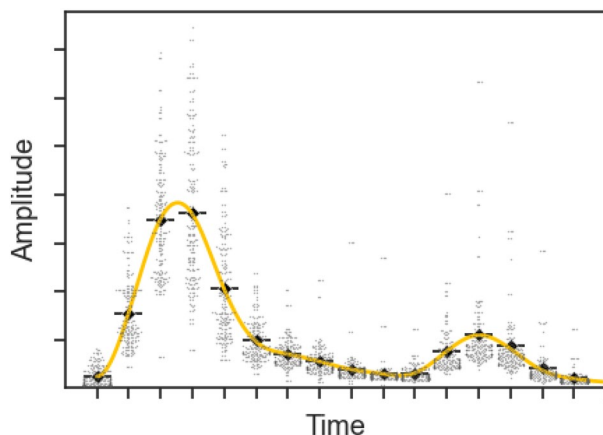
3.1.2 | Curve Fitting

The function used for the laser-water interaction is based on the basic theoretical LiDAR model (Chauve et al. 2007; Schwarz et al. 2017), assuming that the laser pulse is of Gaussian shape and the interaction with the water column introduces an exponential decay component. This is transformed into an empirical model, where we use minimal parameter (Table 2) curve fitting to approximate the reflected echo. For this, we first establish the standard Gaussian pulse as follows:

$$f(t, a, \mu, \sigma) = a \cdot \exp\left(- \frac{(t-\mu)^2}{2\sigma^2} \right) \tag{1}$$
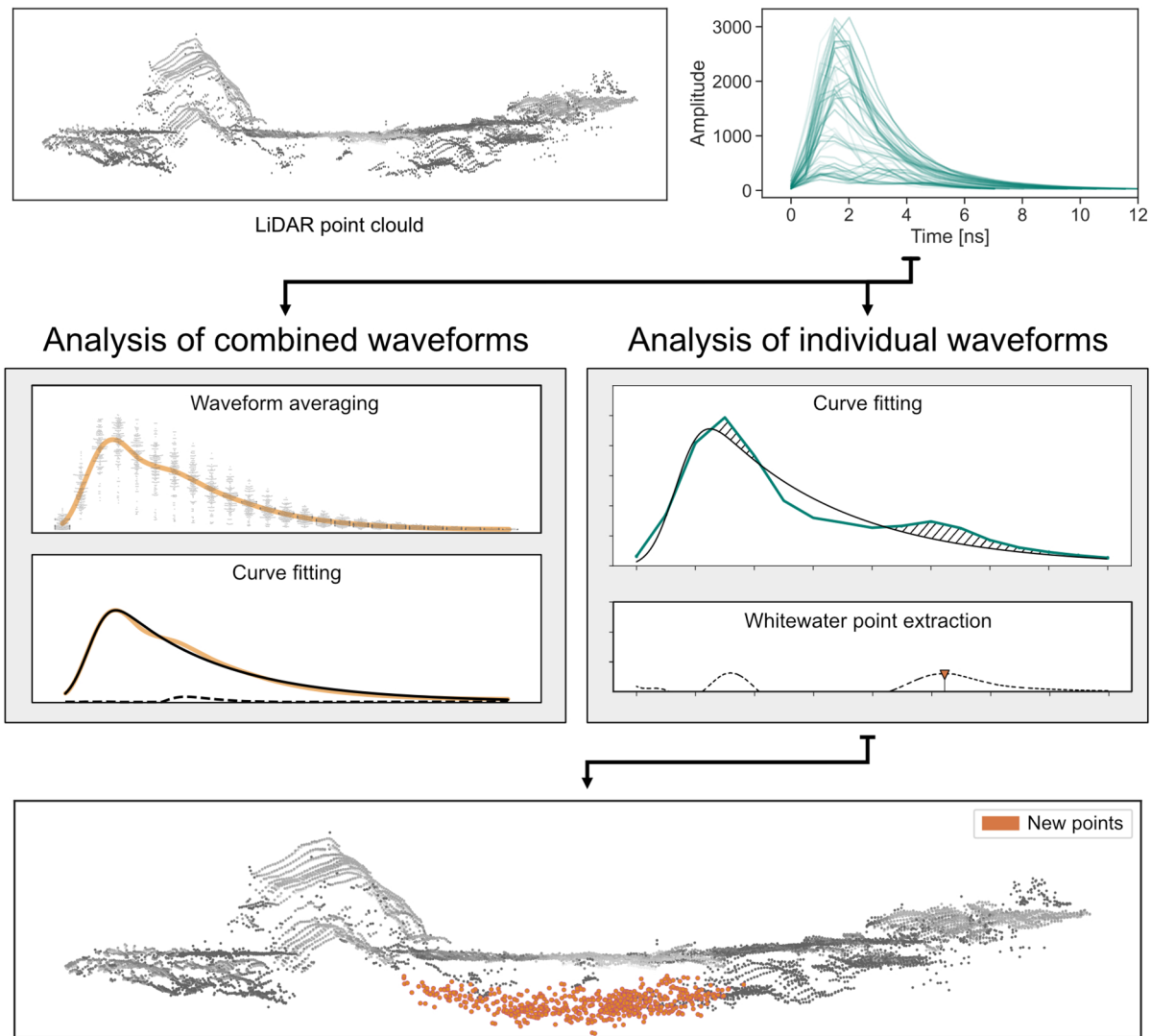
FIGURE 3 | Flowchart outlining the general waveform behavior (analysis of combined waveforms) and the single waveform whitewater point extraction (analysis of individual waveforms) outlined in the methods section. The main difference between the two workflows is that the analysis of combined waveforms uses multiple waveforms as input, while the analysis of individual waveforms is based on each recorded waveform. [Color figure can be viewed at wileyonlinelibrary.com]

and the exponential decay function as follows:

$$\gamma(t, \beta) = \exp(-\beta t). \tag{2}$$

The numerical convolution of these two functions can then be used as a base function for the curve fitting based on the LiDAR waveform. This convolution is given by

$$p_t(a, \mu, \sigma, \beta) = (f * \gamma)(t, a, \mu, \sigma, \beta)$$
$$= \int_0^t f(\xi, a, \mu, \sigma) \cdot \gamma(t - \xi, \beta) \; d\xi. \tag{3}$$

Using nonlinear least squares, this generalized function can now be fitted (Virtanen et al. 2020) to the averaged waveforms to analyze the general behavior of the water column backscatter and the individual waveform in the extraction of whitewater points.

FIGURE 4 | Illustration of the waveform averaging. A scatterplot of the recorded samples (gray) with the mean value in black and the interpolated curve in yellow. The averaged waveform here would correspond to the yellow curve. [Color figure can be viewed at wileyonlinelibrary.com]

3.2 | Analysis of Individual Waveforms

In order to extract bottom returns in the turbulent water of whitewater rapids, we need to differentiate the waveform into the water column backscattering and possible echoes fused within (Figure 5). Initially, recorded waveforms consist of discrete sample intervals approximately every 0.5 ns, and therefore the first step in the whitewater workflow is to interpolate this waveform to a continuous curve. Next, the convolution shown in Equation (3) is fitted to each recorded waveform. In this instance, we did not need to separate the first and secondary echoes, as the whitewater waveforms do not feature the classical second echoes. To compare the interpolated waveform and the fitted curve point-wise, the temporal resolution for both functions is set to a factor of 16 times the recorded sampling rate,

TABLE 2 | Table outlining the different variables for the curve fitting towards the laser-water column-interaction.

Variable	Reference
f	Gaussian pulse
γ	Exponential decay function
p_t	LiDAR-water column-convolution
t	Time (ns)
a	Amplitude (ADC)
μ	Temporal position Gaussian pulse (ns)
σ	Width Gaussian pulse (ns)
β	Backscattering coefficient (—)
ξ	Convolution variable
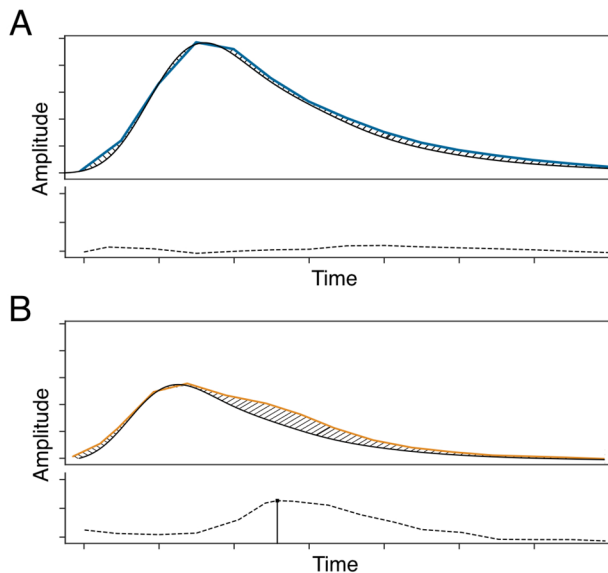
FIGURE 5 | Illustration of two waveforms observed in the whitewater section. High amplitude waveform in blue (A) and low amplitude waveform in orange (B) and the simulated waveform in black. The striped area denotes the difference, which is shown in the lower plots. The difference in panel B displays the potential bottom return extracted from the difference (marked maximum). [Color figure can be viewed at wileyonlinelibrary.com]

as this matches the numerical convolution output (Virtanen et al. 2020) and thus later downsampling can be avoided.

This results in two cases: (i) no fitting is possible (optimal parameters cannot be computed within 250 iterations), which means no further analysis can be done, and no new points are assigned. In the second case (ii), an idealized function representing the water column backscattering can be fitted to the interpolated waveform. We subtract the fitted convolution from the interpolated waveform for each sample and thus get a residual curve for the remaining amplitude. The residual curve now represents the energy not attributed to the water column, and therefore, we can use peak detection to extract potential new echoes. The temporal position of these maxima, together with the recorded beam vector, corresponds to the new terrain points extracted within the whitewater rapid.

We also introduce filter criteria for extracted peaks to improve the signal-to-noise ratio in the data, as the whitewater waveform tends to have deviating shapes from classical bathymetric LiDAR waveforms. Initially, all new points must be later in time than the recorded point of the analyzed waveform (the surface echo), and the method is only applied to waveforms that do not have a second echo (bottom echo). As the mountain rivers are not obstructed by vegetation, this focus on single echoes implies that only water surface echoes were recorded and therefore no distinction between extracted echoes and bottom echoes has to be made.

Furthermore, depending on the depth of the water, a supervised threshold is set to focus on the second peak of the residual curve and a minimum distance from the surface of 20 cm is set to avoid artifacts from the surface of the whitewater (Figure 3). Finally, the points extracted in this manner are cleaned by density-based clustering (Section 2.3) to remove additional false echoes not directly linked to the terrain. This leaves our final set of new points that correspond to the river bottom.

3.3 | Evaluation Methods

To provide an independent reference for the waveform fitting outside the mountain rivers, we evaluate the waveform fitting on a gravel-bed river (the Pielach River). Waveform averaging was used to first create a general function, and secondly, the function is fitted to each individual curve of the averaged waveform. For each waveform, a deviation from the fitting can be calculated, given by the median absolute deviation (MAD) in relation to the maximum amplitude of the waveform.

4 | Results

The results are divided into two sections: the general trends of the recorded waveforms for all three rivers examined with waveform averaging and the extraction of new points in the whitewater rapids, together with the comparison to the reference data.

4.1 | General Waveform Analysis

The first part of the results section focuses on the general behavior of the full-waveform data of a gravel bed river. Waveform

averaging is used to evaluate the waveform fitting for typical gravel bed rivers and shows that there are bottom echoes within the recorded waveform for whitewater rapids.

4.1.1 | Water Column Function

Applying the waveform averaging to the Pielach dataset, we can derive a generalized waveform for the cross section shown in Figure 2. The center-to-right part of the cross section exhibits similar water depths and smooth terrain, as the composition of the ground consists of small gravel, sand, and mud. This, along with the fairly smooth water surface of the river, presents nearly ideal conditions for testing the waveform fitting.

The samples of the selected waveforms, together with the averaged curve as described in Section 3.1.1, can be seen in Figure 6A. The two distinct echoes are clearly visible, the first echo displaying the water surface, followed by subsequent water column backscattering, and the second echo being the bottom return. We focus on the water surface and the subsequent water column backscatter to evaluate the waveform fitting (Figure 6B).
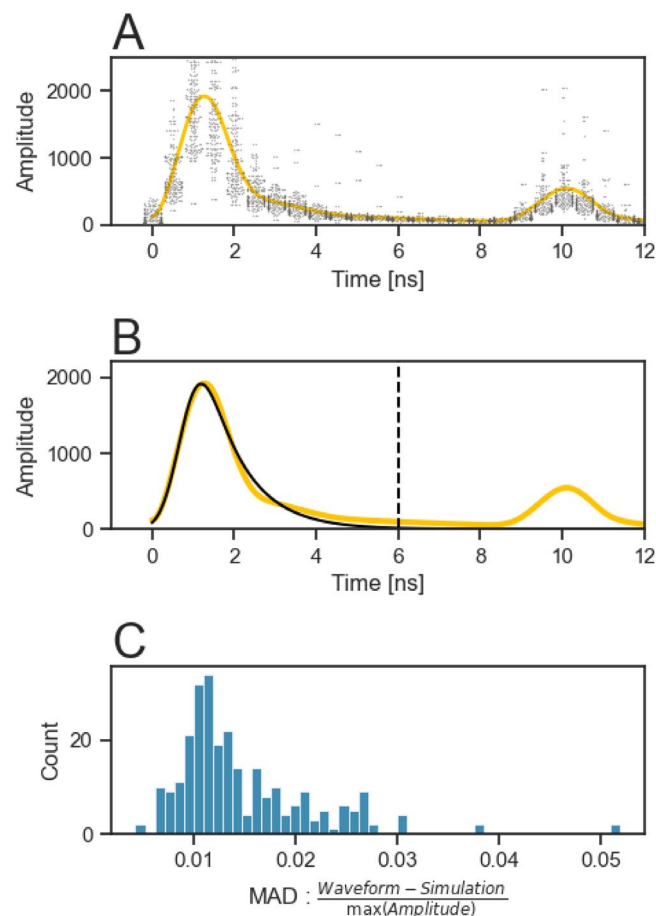
FIGURE 6 | (A) Waveform averaging for the center section of the Pielach River (Figure 2A). (B) Averaged waveform (yellow) and the fitted laser-water column-interaction for the first echo (black), the dashed line is the separation between both echoes. (C) Histogram of the deviation between the curve fitting and the first echo for each waveform in the Pielach dataset, expressed as a percentage of the maximum amplitude. [Color figure can be viewed at wileyonlinelibrary.com]

The black and yellow curves display an overall similar behavior with some degree of variation after the peak. The results of the individual waveform evaluation (Section 3.3) show an offset of around 1% of the maximum amplitude for most curves, with almost all waveforms having less than 3% deviation (Figure 6C).

4.1.2 | Whitewater Waveforms

We empirically separate the waveforms into three categories on the basis of the maximum detected amplitude. Waveforms with an amplitude greater than 2000 ADC display small to no deviation from the fitted curves (Figure 7A,B). For the amplitudes between 1200 and 2000 ADC, the deviation from the waveform fitting is still small (Figure 7D), but has some more visible deviation after the peak (Figure 7C). Lastly, the waveforms with an amplitude lower than 1200 ADC have a visible deviation after the peak of the waveform, similar to a second echo engulfed in the water column backscatter of the water surface (Figure 7E,F).

Based on these differences (dashed lines, Figure 7), the extraction of the new points outlined in Section 3.2 becomes evident. Especially in Panels E and F of Figure 7, the residual exhibits a small secondary echo that can be used for peak detection to provide additional points within the whitewater rapids.

4.2 | Single Waveform Whitewater Point Extraction

The second part of the results section focuses on the whitewater point extraction based on individual waveforms. We compare the newly derived whitewater bottom points with the reference measurements for both mountain rivers with a focus on the improvements in accuracy and point density.

4.2.1 | Whitewater Bottom Points

The results of the whitewater bottom point extraction (Section 3.2) can be seen in Figure 8, where the four panels show the introduced cross sections (Section 2) before and after the method is applied.

In both sections, the turbulent whitewater results in few or no bottom returns even with advanced processing such as SVB, which is directly visible when comparing the river cross section for both the Passer and Fischbach River with the acquired reference data for each cross section (Figure 8A,C). After applying the introduced workflow, both sections show an increase in bottom returns (Figure 8B,D), which match the acquired reference data to some extent. Furthermore, Figure 8B,D shows the difference between the new points and the outliers removed by the last clustering step of the method. In both cross sections, the points classified as outliers are towards the waterline of the whitewater section, as there the density of the new points decreases. Thus, the clustering-based outlier removal helps avoid false echoes in the transition area of the land-water boundary.

In contrast to the standard processing, the newly added points display a high degree of noise, which can be seen in the
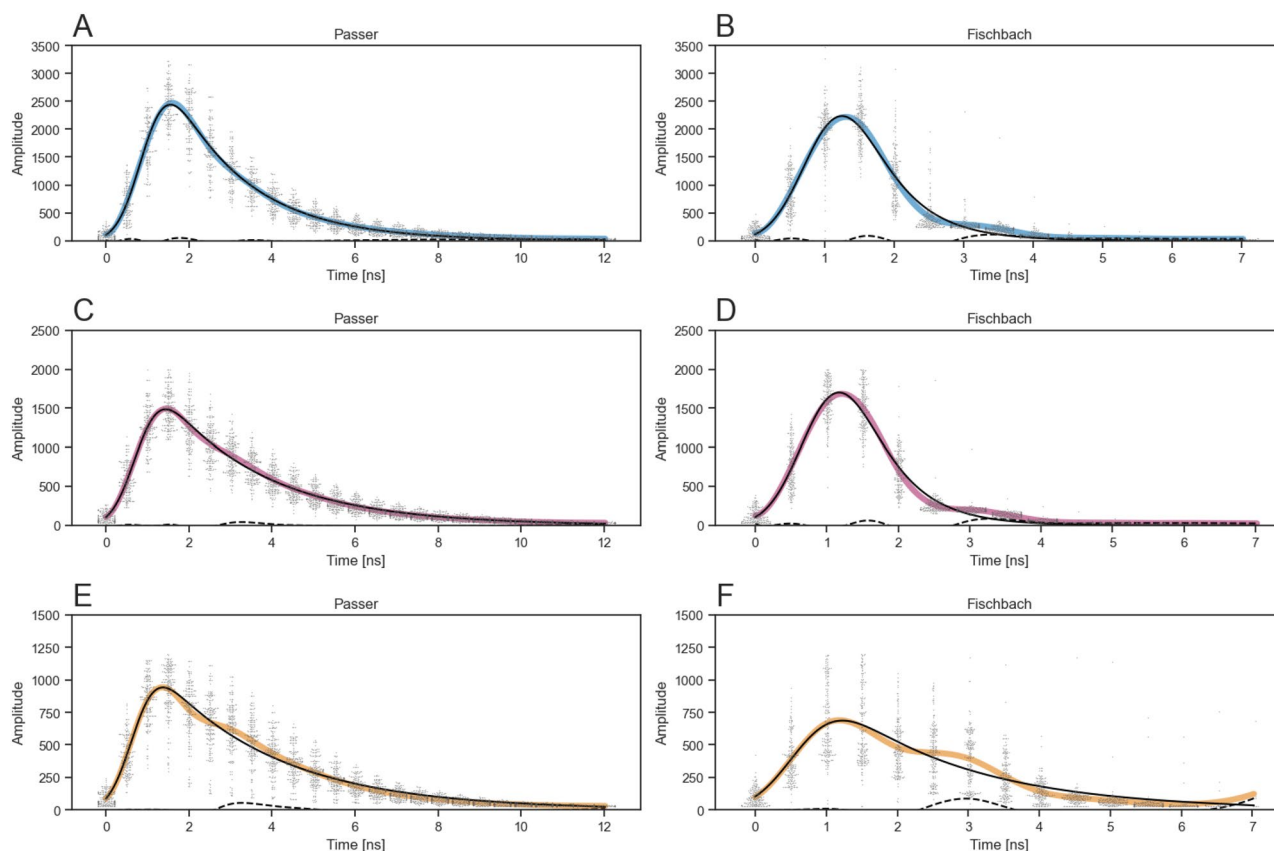
FIGURE 7 | Waveform averaging plots for different amplitude ranges for the Passer and Fischbach River. (A and B) Waveform averaging for waveforms with a maximum amplitude greater 2000 ADC. (C and D) Waveform averaging for waveforms with a maximum amplitude between 1200 and 2000 ADC. (E and F) Waveform averaging for waveforms with a maximum amplitude less then 1200 ADC. [Color figure can be viewed at wileyon-linelibrary.com]

varying vertical positions of the added data. Therefore, fur-ther quantitative analysis is required to assess the accuracy of the extracted points in relation to the collected reference measurements.

4.2.2 | Comparison to Reference Data

To evaluate the new points, we compare the measured reference data with the nearest neighbor in the point cloud and calculate the vertical difference between the two points. This is done for point-wise distances of up to 1 m to exclude reference data ac-quired outside the river.

For the Pielach River control dataset, this leads to a minimum absolute deviation of 0.2 cm and a maximum absolute deviation of 6.2 cm for the selected cross section (Table 3). For the Pielach River, a rigorous registration of the point cloud on the refer-ence measurements was performed using reference planes. For the mountain rivers, the poor GNSS signal quality, due to the mountainous environment, in combination with a less precise registration approach, leads to higher registration errors. This leaves the Pielach dataset with subcentimeter accuracy and the mountain river dataset with mean point accuracies between 9.2 and 22.5 cm (Table 3).

For the two mountain rivers, the vertical distances to the ref-erence data for the cross sections can be seen in Table 3, before

and after the new points were added. For both mountain riv-ers, there is a notable decrease in the vertical distances to the reference data after the application of the new method. For the Passer river, the mean and median accuracies improve by 11.4 and 4.9 cm. Similarly, for the Fischbach River, the accuracies im-prove by 17.9 and 14.2 cm.

For each river, multiple transects were acquired (Figure 9A,C), and the vertical distances can be calculated before and after the applied method. The results can be seen in Figure 9B,D. Furthermore, the results are given as numerical values of the mean and median distance in Table 3. There, a mean and me-dian shift improvement of more than 15 cm can be seen, show-ing an overall accuracy improvement in the data (Table 3) and, together with the results of Figure 8, highlighting the successful capture of bottom echoes in whitewater rapids.

In addition to the improvement in accuracy, the whitewater bottom points increase the overall point density by 12% for the Passer River and 27% for the Fischbach River, before the clustering-based filtering. The increase in density is calculated based on the initial points of the point cloud, limited to the man-ually annotated underwater terrain. For the underwater terrain, the points per square meter thus increased by 24 points/m² for the Passer River and 33 points/m² for the Fischbach River.

The lower increase in point density compared to the signifi-cant improvement in the mean and median distance from the
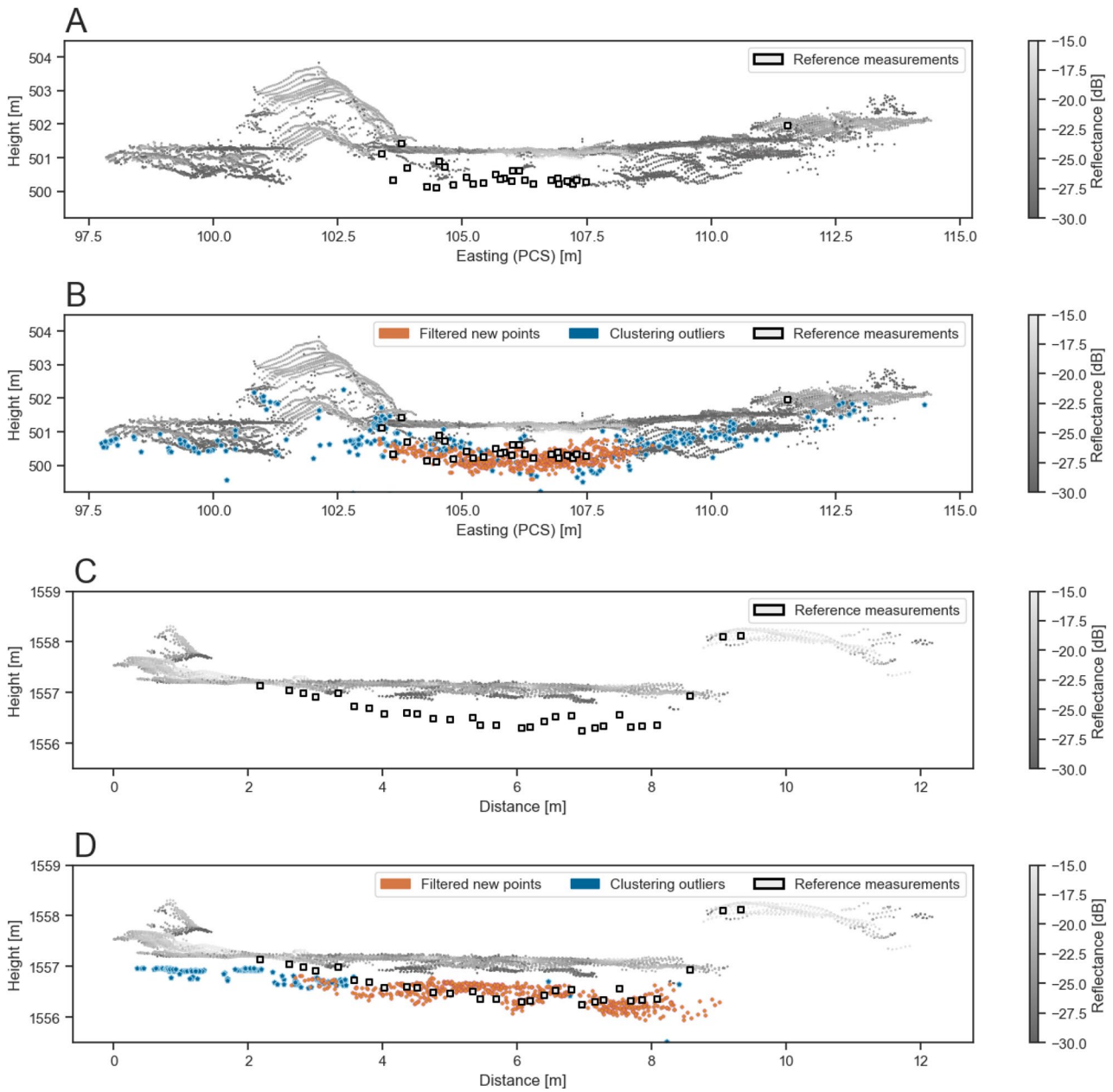
FIGURE 8 | Cross section plots of the (A, B) Passer and (C, D) Fischbach River (Figure 2) before and after the whitewater point extraction. Each plot displays, in addition to the LiDAR data, the measured reference data (gray boxes). [Color figure can be viewed at wileyonlinelibrary.com]

TABLE 3 | Table displaying the mean and median absolute vertical distances for each cross section and the total surveyed area (Figures 8 and 9).

Location	Mean distance before	Median distance before	Mean distance after	Median distance after
Pielach cross section	3.8 cm	4.3 cm	—	—
Passer cross section	41.7 cm	39.0 cm	13.2 cm	11.0 cm
Fischbach cross section	36.8 cm	39.5 cm	10.0 cm	7.8 cm
Passer	20.6 cm	12.3 cm	9.2 cm	7.4 cm
Fischbach	40.4 cm	37.7 cm	22.5 cm	13.5 cm

reference data is caused by the data gaps (Figure 1). In the whitewater rapids, standard processing resulted in a limited number of bottom points; thus, the nearest neighbor within

the defined search radius is often further away than the actual bottom. In the less turbulent sections, consistent bottom echoes could be extracted without the whitewater point
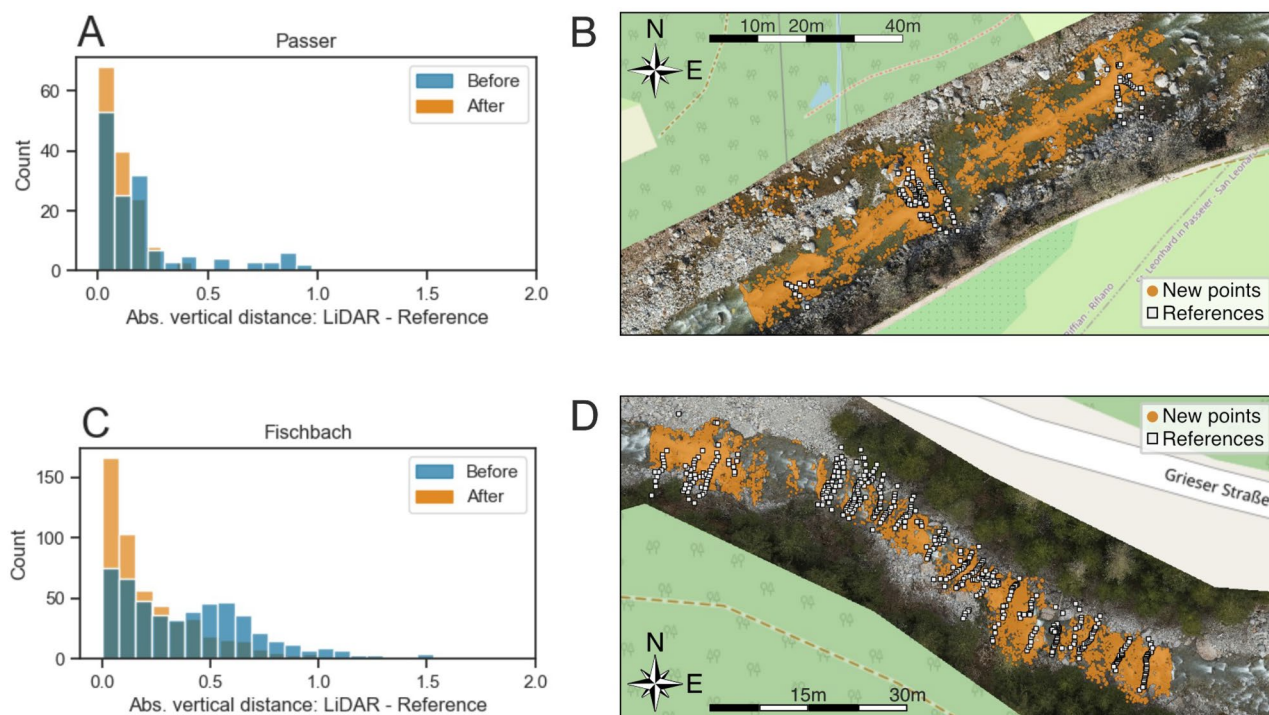
FIGURE 9 | Evaluation of the complete river section surveyed. (A and B) Histograms of the absolute vertical distances to the reference measurements for the Passer and the Fischbach River. "Before" refers to the initial LiDAR data, and "After" to the improvement through adding the whitewater points. (C and D) Orthophotos and map overview (OpenStreetMap Contributors 2017) of the two rivers with the new whitewater points in orange and the reference in grey. [Color figure can be viewed at wileyonlinelibrary.com]

extraction method (Figure 8). Therefore, the new whitewater points produced a substantial decrease in the distance to the reference points.

5 | Discussion

Our study shows that we were able to capture bottom echoes in whitewater sections of rivers with our method. However, concerns remain regarding the high degree of noise and overall deviation from the acquired reference data compared to standard bathymetric LiDAR accuracies. Therefore, the following section aims to evaluate the challenges in collecting reference data, outline possible improvements for future work, and critically discuss the results presented.

5.1 | Reference Data Acquisition

The difficult environment of mountain rivers imposes various obstacles on the acquisition of high-precision reference data. These include the higher uncertainty of GNSS measurements in mountainous environments and the fluctuating accuracy of the reference measurements due to the high flow velocities acting on the surveyor and the uneven terrain of the rivers, where varying boulder sizes lead to large vertical fluctuation during the transect measurements.

The first source of discrepancies is the georeferencing. The typical approach is to use GNSS measurements to transform the local PCS in a global coordinate system (GCS) to align both LiDAR and reference measurements within the same coordinate system (Nesbit et al. 2022; Mohamed and Wilkinson 2009). In normal measurement environments, this is done by ground control points, measured with GNSS (Mohamed and Wilkinson 2009; Stott et al. 2020), but in mountainous environments, the satellite signal obstruction from the surrounding topography leads to less accurately measured ground control points. In the case of the Fischbach dataset, the georeferencing using ground control points was insufficient. Thus, we improved the georeferencing by using fixed features in the area (e.g., roads, tunnels, etc.) to account for differences between the PCS and the GCS for the selected ground control points. For these points, we see a vertical standard deviation of 2.4 cm, which is part of the potential deviation in the evaluation. As for the Passer River, the data was referenced to a preexisting height control point, since the total station measurements and LiDAR data displayed discrepancies of up to 10 cm before aligning the dataset.

Second, the reference measurement itself poses a challenge on its own, as the flow velocity in whitewater rapids is significantly higher and can, depending on the river morphology, reach values above 3 m/s (Magirl et al. 2009). Not only does the surveyor have to maintain a stable position in a highly turbulent flow and uneven terrain, but also has to keep the measurement pole with the mounted reflector as steady as possible to avoid inaccuracies in the measurement itself. This, in combination with the heterogeneous terrain, where small changes to the measured position constitute larger changes in the depth due to the rough nature of the river bed, leads to additional uncertainties in the reference data.

Finally, for the mountain river datasets, there is a chance of changes in the river topography, since the initial LiDAR measurements were conducted in March and April 2024, while the references were measured in December 2024 and January 2025. According to the gauge data available on each mountain river, both river sections experienced a flood event with a one-year return interval. However, the reference data at the whitewater rapid locations was predominantly taken from large immobile rock boulders. However, this could be overcome in future work with better planning during the low-flow season, allowing both types of measurements to be done at the same time.

The effect of these influences on the measurement can be seen in relation to the Pielach dataset, where a standard case for river bathymetry is displayed. The measurement accuracy to the reference was between 0.2 and 6.2 cm, where the mean deviation was 3.8 cm with a standard deviation of 1.6 cm. Furthermore, in the Pielach River dataset, the accuracy was additionally improved through saddle roof references, which allowed for a more accurate referencing of the LiDAR data to the reference data (Mandlburger et al. 2025). Therefore, the lower precision of the new points calculated in the mountain river environment does not necessarily reflect poor results but is strongly influenced by the challenging environment of mountain rivers for reference data collection. Therefore, for a more detailed evaluation, further reference would be required with a more extensive measurement, ideally in a more controlled environment such as fish steps near dams or in a laboratory.

5.2 | Waveform Processing

Another aspect with respect to the quality of the calculated whitewater points is the method used for the simulation of the laser-water column interaction and the echo extraction. For the water column backscattering simulation, different functions can be used for the initial laser pulse, such as a heavy-tailed curve (Rhomberg-Kauert, Pöppl, et al. 2024; Shen et al. 2017) or a more system-tailored function (Schwarz et al. 2017; Yang et al. 2023). These could more accurately represent the water column backscattering, leading to an improved residual. However, we decided on our minimalistic waveform fitting approach to avoid overfitting.

Similarly, for the echo extraction from the residual signal, we use standard peak detection, which does not necessarily correspond to the exact temporal position of the target. The method could be improved through different curve fitting techniques or power thresholds to better estimate the temporal position (Chauve et al. 2007; Schwarz et al. 2019).

5.3 | Relevance for River Applications

Topo-bathymetric LiDAR applications for whitewater rivers were previously considered difficult or even impossible (Awadallah et al. 2023; Kastdalen et al. 2024; Lague and Feldmann 2020). Topo-bathymetric LiDAR did not appear to be able to provide continuous spatial data on the topography of the riverbed, which meant that data gaps had to be ignored or filled using other techniques (Wiener and Pasternack 2022). In particular, the bathymetry of mountain rivers, with their highly variable riverbed structure, has a decisive influence on the flow process and thus on sediment transport. Consequently, a high spatial resolution is necessary to model the riverbed appropriately. If data gaps cannot be closed by additional survey measurements (e.g., GNSS or total station), as is the case with inaccessible turbulent whitewater sections in mountain rivers (Strom et al. 2017), data interpolation reduces the reliability of the results of hydro- and morphodynamic as well as ecological river basin studies (Farò et al. 2023; Kinzel et al. 2012). With the outlined processing method, data gaps can be reduced and the entire field of topo-bathymetric LiDAR applications could be extended to more complex river applications (Ferguson et al. 2024). However, the outlined improvements remain to be tested in future research, but the method highlights the potential of applying topo-bathymetric LiDAR to whitewater rivers. Thus, it is shown that this topic holds great value for further experiments and surveys on the accuracy and potential of bathymetric LiDAR in mountain river environments.

6 | Conclusion

The study of whitewater rivers, in particular with remote-sensing data, has long been regarded as challenging. With the application of recent advances in bathymetric full-waveform LiDAR and on the basis of our datasets, we present a case study for mapping such environments, at least to a degree of uncertainty. Through the introduction of waveform averaging for both gravel-bed and mountain rivers, we have shown that the curve fitting approach reflects an idealized laser-water interaction, and there are echoes within the whitewater waveforms not detected by standard LiDAR waveform processing. Furthermore, single-waveform-based whitewater point extraction is able to detect bottom returns within the rapids through the subtraction of an idealized water column backscattering, leading to a residual, where peak detection can extract additional echoes. These points have shown a mean vertical distance of 7.8 cm to 9.5 cm to the acquired reference data, while the initial point clouds without the whitewater bottom points showed a mean deviation of over 35 cm. However, the reference measurements and georeferencing are not without challenges, and future research should implement a more rigorous georeferencing framework. In conclusion, our method successfully improves terrain detection in whitewater sections and overcomes a major challenge in mountain river surveying, thus improving the general topo-bathymetric LiDAR signal processing and opening up new possibilities for hydraulic research and modeling.

Conflicts of Interest

The authors declare no conflicts of interest.

Data Availability Statement

The data that support the findings of this study are available from the corresponding author upon reasonable request.

References

Awadallah, M. O. M., C. Malmquist, M. Stickler, and K. Alfredsen. 2023. "Quantitative Evaluation of Bathymetric Lidar Sensors and Acquisition Approaches in Lærdal River in Norway." *Remote Sensing* 15, no. 1: 263.

Bio, A., J. Gonçalves, A. Magalhães, J. Pinheiro, and L. Bastos. 2020. "Combining Low-Cost Sonar and High-Precision Global Navigation Satellite System for Shallow Water Bathymetry." *Estuaries and Coasts* 45: 1–12.

Blöschl, G. 2024. "September 2024 Flooding in Central Europe: The Austrian Experience." EGU Blogs, GeoLog. https://blogs.egu.eu/geo-log/2024/09/26/september-2024-flooding-in-central-europe-the-austrian-experience.

Buffington, J. M., and D. R. Montgomery. 2021a. "Geomorphic Classification of Rivers: An Updated Review." In *Treatise on Geomorphology*, vol. 2, 1–47. Academic Press.

Bundesamt für Eich- und Vermessungswesen (BEV). 2024. "Austrian Map Online." https://www.bev.gv.at/Services/Produkte/Austrian-Map/Austrian-Map-online.html.

Chauve, A., C. Mallet, F. Bretar, et al. 2007. "Processing Full-Waveform Lidar Data: Modelling Raw Signals." *International Archives of Photogrammetry, Remote Sensing and Spatial Information Sciences* 36, no. 3: W52.

Dey, S., S. Saksena, and V. Merwade. 2019. "Assessing the Effect of Different Bathymetric Models on Hydraulic Simulation of Rivers in Data Sparse Regions." *Journal of Hydrology* 575: 838–851.

Dietrich, J. T. 2016. "Riverscape Mapping With Helicopter-Based Structure-From-Motion Photogrammetry." *Geomorphology* 252: 144–157.

Dufficy, A. L., B. C. Eaton, and R. D. Moore. 2024. "Quantifying Hydraulic Geometry and Whitewater Coverage for Steep Proglacial Streams to Support Process-Based Stream Temperature Modelling." *Hydrological Processes* 38, no. 11: e70003.

Ester, M., H.-P. Kriegel, J. Sander, et al. 1996a. "A Density-Based Al0 Spatial Databases With Noise." In *KDD'96: Proceedings of the Second International Conference on Knowledge Discovery and Data Mining*, 226–231. AAAI Press.

Farò, D., K. Baumgartner, P. Vezza, and G. Zolezzi. 2023. "Sensitivity of Fish Habitat Suitability to Multi-Resolution Hydraulic Modeling and Field-Based Description of Meso-Scale River Habitats." *Journal of Hydrology X* 21: 100160.

Ferguson, R. I., R. J. Hardy, R. A. Hodge, R. C. Houseago, E. M. Yager, and T. N. Yamasaki. 2024. "Predicting Flow Resistance in Rough-Bed Rivers From Topographic Roughness: Review and Open Questions." *Earth Surface Processes and Landforms* 49, no. 15: 4888–4907.

Frizzle, C., M. Trudel, S. Daniel, A. Pruneau, and J. Noman. 2024. "LiDAR Topo-Bathymetry for Riverbed Elevation Assessment: A Review of Approaches and Performance for Hydrodynamic Modelling of Flood Plains." *Earth Surface Processes and Landforms* 49: 2585–2600.

Hall, R. O., T. A. Kennedy, and E. J. Rosi-Marshall. 2012. "Air–Water Oxygen Exchange in a Large Whitewater River." *Limnology and Oceanography: Fluids and Environments* 2, no. 1: 1–11.

Hartmann, K., E. Albada, and T. Heege. 2021. "Latest Developments in Satellite Derived Bathymetry: Technology, Use Cases and Tools." In *OCEANS 2021: San Diego–Porto*, 1–7. IEEE.

Jawak, S. D., S. S. Vadlamani, and A. J. Luis. 2015. "A Synoptic Review on Deriving Bathymetry Information Using Remote Sensing Technologies: Models, Methods and Comparisons." *Advances in Remote Sensing* 4, no. 2: 147–162.

Kastdalen, L., M. Stickler, C. Malmquist, and J. Heggenes. 2024. "Evaluating Methods for Measuring In-River Bathymetry: Remote Sensing Green Lidar Provides High-Resolution Channel Bed Topography Limited by Water Penetration Capability." *River Research and Applications* 40, no. 4: 467–482.

Kim, Y., and J. Ryou. 2020. "A Study of Sonar Image Stabilization of Unmanned Surface Vehicle Based on Motion Sensor for Inspection of Underwater Infrastructure." *Remote Sensing* 12, no. 21: 3481.

Kinzel, P. J., C. J. Legleiter, and P. E. Grams. 2021. "Field Evaluation of a Compact, Polarizing Topo-Bathymetric Lidar Across a Range of River Conditions." *River Research and Applications* 37, no. 4: 531–543.

Kinzel, P. J., C. J. Legleiter, and J. M. Nelson. 2012. "Mapping River Bathymetry With a Small Footprint Green Lidar: Applications and Challenges." *JAWRA Journal of the American Water Resources Association* 49, no. 1: 183–204.

Lague, D., and B. Feldmann. 2020. *Topo-Bathymetric Airborne LiDAR for Fluvial-Geomorphology Analysis Developments in Earth Surface Processes*. Vol. 23, 25–54. Elsevier.

Lee, C.-H., L.-W. Liu, Y.-M. Wang, J.-M. Leu, and C.-L. Chen. 2022. "Drone-Based Bathymetry Modeling for Mountainous Shallow Rivers in Taiwan Using Machine Learning." *Remote Sensing* 14, no. 14: 3343.

Li, R., L. Montano, K. Splinter, and S. Felder. 2019. "Opportunities of Lidar Measurements in Air-Water Flows." In *38th IAHR World Congress—"Water: Connecting the World"*, vol. 38, 5693–5703. International Association for Hydro-Environment Engineering and Research (IAHR).

Li, R., K. D. Splinter, and S. Felder. 2022a. "Lidar Measurements of Air-Water Flows in a Creek." In *Proceedings of the 39th IAHR World Congress*, 19–24. International Association for Hydro-Environment Engineering and Research (IAHR).

Mader, D., K. Richter, P. Westfeld, and H.-G. Maas. 2021. "Potential of a Non-Linear Full-Waveform Stacking Technique in Airborne Lidar Bathymetry: Demonstration of Full-Waveform Stacking Techniques on Data From the Elbe River." *PFG—Journal of Photogrammetry, Remote Sensing and Geoinformation Science* 89, no. 2: 139–158.

Magirl, C. S., J. W. Gartner, G. M. Smart, and R. H. Webb. 2009. "Water Velocity and the Nature of Critical Flow in Large Rapids on the Colorado River, Utah." *Water Resources Research* 45, no. 5.

Mallet, C., and F. Bretar. 2009. "Full-Waveform Topographic Lidar: State-of-the-Art." *ISPRS Journal of Photogrammetry and Remote Sensing* 64, no. 1: 1–16.

Mandlburger, G., C. Hauer, B. Höfle, H. Habersack, and N. Pfeifer. 2009. "Optimisation of Lidar Derived Terrain Models for River Flow Modelling." *Hydrology and Earth System Sciences* 13, no. 8: 1453–1466.

Mandlburger, G., C. Hauer, M. Wieser, and N. Pfeifer. 2015. "Topo-Bathymetric Lidar for Monitoring River Morphodynamics and Instream Habitats—A Case Study at the Pielach River." *Remote Sensing* 7, no. 5: 6160–6195.

Mandlburger, G., M. Pfennigbauer, R. Schwarz, and F. Pöppl. 2023. "A Decade of Progress in Topo-Bathymetric Laser Scanning Exemplified by the Pielach River Dataset." *ISPRS Annals of the Photogrammetry, Remote Sensing and Spatial Information Sciences* 10: 1123–1130.

Mandlburger, G., J. Rhomberg-Kauert, L.-A. Gueguen, et al. 2025. "Mapping Shallow Inland Running Waters With UAV-Borne Photo and Laser Bathymetry." *Hydrographische Nachrichten*, no. 130: 42–54.

McMahon, J. 1981. *Maine's Whitewater Rapids and Their Relevance to the Critical Areas Program*. Planning Report No. 74. Critical Areas Program.

Mohamed, A., and B. Wilkinson. 2009. "Direct Georeferencing of Stationary Lidar." *Remote Sensing* 1, no. 4: 1321–1337.

Moramarco, T., S. Barbetta, D. M. Bjerklie, J. W. Fulton, and A. Tarpanelli. 2019. "River Bathymetry Estimate and Discharge Assessment From Remote Sensing." *Water Resources Research* 55, no. 8: 6692–6711.

Nesbit, P. R., S. M. Hubbard, and C. H. Hugenholtz. 2022. "Direct Georeferencing UAV-SfM in High-Relief Topography: Accuracy Assessment and Alternative Ground Control Strategies Along Steep Inaccessible Rock Slopes." *Remote Sensing* 14, no. 3: 490.

OpenStreetMap Contributors. 2017. "Planet Dump." https://www.openstreetmap.org.

Pagliara, S., I. Lotti, and M. Palermo. 2008. "Hydraulic Jump on Rough Bed of Stream Rehabilitation Structures." *Journal of Hydro-Environment Research* 2, no. 1: 29–38.

Pan, Z., C. Glennie, P. Hartzell, J. Fernandez-Diaz, C. Legleiter, and B. Overstreet. 2015. "Performance Assessment of High Resolution Airborne Full Waveform Lidar for Shallow River Bathymetry." *Remote Sensing* 7, no. 5: 5133–5159.

Pan, Z., C. Glennie, C. Legleiter, and B. Overstreet. 2015. "Estimation of Water Depths and Turbidity From Hyperspectral Imagery Using Support Vector Regression." *IEEE Geoscience and Remote Sensing Letters* 12, no. 10: 2165–2169.

Panchan, R., K. Pinter, S. Schmutz, and G. Unfer. 2022. "Seasonal Migration and Habitat Use of Adult Barbel (*Barbus barbus*) and Nase (*Chondrostoma nasus*) Along a River Stretch of the Austrian Danube River." *Environmental Biology of Fishes* 105, no. 11: 1601–1616.

Papadaki, C., K. Soulis, R. Muñoz-Mas, et al. 2016. "Potential Impacts of Climate Change on Flow Regime and Fish Habitat in Mountain Rivers of the South-Western Balkans." *Science of the Total Environment* 540: 418–428.

Pedregosa, F., G. Varoquaux, A. Gramfort, et al. 2011. "Scikit-Learn: Machine Learning in Python." *Journal of Machine Learning Research* 12: 2825–2830.

Pfennigbauer, M., P. Rieger, R. Schwarz, and A. Ullrich. 2022. "Impact of Beam Parameters on the Performance of a Topo-Bathymetric Lidar Sensor." In *Laser Radar Technology and Applications XXVII*, vol. 12110, 107–117. SPIE.

Pfennigbauer, M., P. Rieger, N. Studnicka, and A. Ullrich. 2009. "Detection of Concealed Objects With a Mobile Laser Scanning System." *Proceedings of SPIE, the International Society for Optical Engineering* 7323: 51–59.

Pfennigbauer, M., A. Ullrich, F. Steinbacher, and M. Aufleger. 2011. "High-Resolution Hydrographic Airborne Laser Scanner for Surveying Inland Waters and Shallow Coastal Zones." In *Laser Radar Technology and Applications XVI*, edited by M. D. Turner and G. W. Kamerman, vol. 8037, 803706. SPIE.

Piégay, H., F. Arnaud, B. Belletti, et al. 2019. "Remotely Sensed Rivers in the Anthropocene: State of the Art and Prospects." *Earth Surface Processes and Landforms* 45: 157–188.

Rhomberg-Kauert, J., L. Dammert, M. Groemer, M. Pfennigbauer, and G. Mandlburger. 2024. "Macrophyte Detection With Bathymetric Lidar – Applications of High-Dimensional Data Analysis for Submerged Ecosystems." *International Hydrographic Review* 30, no. 2: 98–115.

Rhomberg-Kauert, J., L. Dammert, M. Grömer, M. Pfennigbauer, and G. Mandlburger. 2025. "Optical Hydrography for Seasonal and Flood-Induced Changes in Aquatic Vegetation." In *The International Archives of the Photogrammetry, Remote Sensing and Spatial Information Sciences*, vol. XLVIII-2/W10-2025, 239–246.

Rhomberg-Kauert, J., F. Pöppl, M. Pfennigbauer, and G. Mandlburger. 2024. "Estimation of the Angle of Incidence Based on Echo Pulse Width in Airborne Lidar." In *Wissenschaftlich-Technische Jahrestagung Der DGPF in Remagen—Publikationen Der DGPF*, vol. 32, 67–76. DGPF.

Schubert, E., J. Sander, M. Ester, H. P. Kriegel, and X. Xu. 2017. "DBSCAN Revisited, Revisited: Why and How You Should (Still) Use DBSCAN." *ACM Transactions on Database Systems* 42, no. 3: 1–21.

Schwarz, R., G. Mandlburger, M. Pfennigbauer, and N. Pfeifer. 2019. "Design and Evaluation of a Full-Wave Surface and Bottom-Detection Algorithm for Lidar Bathymetry of Very Shallow Waters." *ISPRS Journal of Photogrammetry and Remote Sensing* 150: 1–10.

Schwarz, R., N. Pfeifer, M. Pfennigbauer, and A. Ullrich. 2017. "Exponential Decomposition With Implicit Deconvolution of Lidar Backscatter From the Water Column." *PFG—Journal of Photogrammetry, Remote Sensing and Geoinformation Science* 85, no. 3: 159–167.

Schwarz, R., and M. Pfennigbauer. 2024. "Pre-Detection and Pre-Registration Averaging of Full Wave Signals in Airborne Lidar Bathymetry." *Remote Sensing* 16, no. 20: 3827.

Shen, X., Q.-Q. Li, G. Wu, and J. Zhu. 2017. "Decomposition of Lidar Waveforms by b-Spline-Based Modeling." *ISPRS Journal of Photogrammetry and Remote Sensing* 128: 182–191.

Skinner, K. D. 2011. *Evaluation of Lidar-Acquired Bathymetric and Topographic Data Accuracy in Various Hydrogeomorphic Settings in the Deadwood and South Fork Boise Rivers, West-Central Idaho, 2007*. Technical Report. US Geological Survey.

Stott, E., R. D. Williams, and T. B. Hoey. 2020. "Ground Control Point Distribution for Accurate Kilometre-Scale Topographic Mapping Using an RTK-GNSS Unmanned Aerial Vehicle and SfM Photogrammetry." *Drones* 4, no. 3: 55.

Strom, M. A., G. B. Pasternack, S. G. Burman, H. E. Dahlke, and S. Sandoval-Solis. 2017. "Hydraulic Hazard Exposure of Humans Swept Away in a Whitewater River." *Natural Hazards* 88, no. 1: 473–502.

Sundt, H., K. Alfredsen, and A. Harby. 2021. "Regionalized Linear Models for River Depth Retrieval Using 3-Band Multispectral Imagery and Green LIDAR Data." *Remote Sensing* 13, no. 19: 3897.

Tomsett, C., and J. Leyland. 2019. "Remote Sensing of River Corridors: A Review of Current Trends and Future Directions." *River Research and Applications* 35, no. 7: 779–803.

Tonina, D., J. McKean, R. Benjankar, et al. 2020. "Evaluating the Performance of Topobathymetric LiDAR to Support Multi-Dimensional Flow Modelling in a Gravel-Bed Mountain Stream." *Earth Surface Processes and Landforms* 45, no. 12: 2850–2868.

Ullrich, A., and R. Reichert. 2005. "High Resolution Laser Scanner With Waveform Digitization for Subsequent Full Waveform Analysis." In *Laser Radar Technology and Applications X*, edited by G. W. Kamerman, vol. 5791, 82–88. SPIE.

Virtanen, P., R. Gommers, T. E. Oliphant, et al. 2020. "SciPy 1.0: Fundamental Algorithms for Scientific Computing in Python." *Nature Methods* 17: 261–272.

Wheaton, J. M., J. Brasington, S. E. Darby, et al. 2009. "Linking Geomorphic Changes to Salmonid Habitat at a Scale Relevant to Fish." *River Research and Applications* 26, no. 4: 469–486.

Wiener, J. S., and G. B. Pasternack. 2022. "Scale Dependent Spatial Structuring of Mountain River Large Bed Elements Maximizes Flow Resistance." *Geomorphology* 416: 108431.

Wohl, E., S. N. Lane, and A. C. Wilcox. 2015. "The Science and Practice of River Restoration." *Water Resources Research* 51, no. 8: 5974–5997.

Woodget, A. S., R. Austrums, I. P. Maddock, and E. Habit. 2017. "Drones and Digital Photogrammetry: From Classifications to Continuums for Monitoring River Habitat and Hydromorphology." *WIREs Water* 4, no. 4: e1222.

Yang, F., C. Qi, D. Su, et al. 2023. "Modeling and Analyzing Water Column Forward Scattering Effect on Airborne Lidar Bathymetry." *IEEE Journal of Oceanic Engineering* 48: 1373–1388.